Chapter 5

MODIFIED CRAM'S THEORY AND ITS DEPENDENCE ON VARIOUS PARAMETERS

5.1 Modified Cram's theory

Lawrence Cram (1976) formulated the theory for the formation of the K-corona. The modified Cram's theory includes the influence of the solar wind velocity in the formation of the K-corona, which is a continuous spectrum. The reasons for the formation of this continuous spectrum and the influence of the solar wind velocity are discussed in chapter-**2**. Figure (**5.1**) is a schematic diagram showing the mathematical description of the scattering phenomenon where the photospheric radiation from the sun is scattered by the free electrons lying along the line of sight of an observer. This scattering phenomenon is popularly known as Thomson scattering while the scattered radiation contributes to the formation of the K-corona. A detailed treatment of the scattered intensity, which includes the influence of the solar wind velocity, is provided in Appendix-**A**. Equation (**5.1**) gives the intensity of the radiation scattered at an observed wavelength (λ) by the free electron density distribution along the line of sight at height (ρ) above the solar limb.

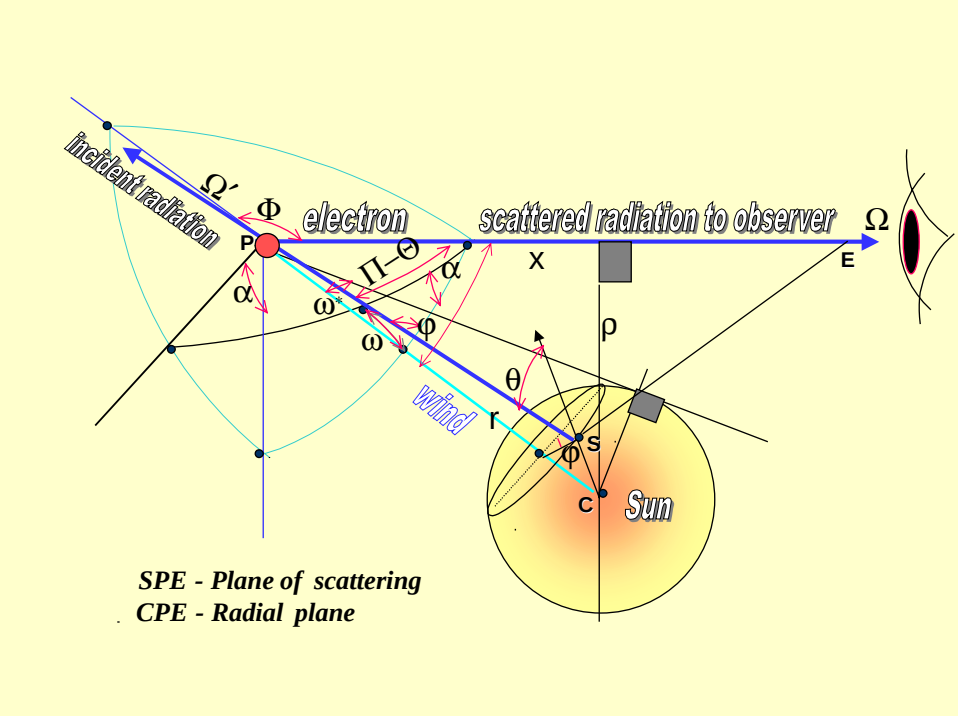

Figure (5.1). This is a schematic diagram showing the mathematical description of the scattering phenomenon where the photospheric radiation from the sun is scattered by the free electrons lying along the line of sight of an observer. The line of sight is at a distance (ρ) from the center of the sun.

$$I_O^{Ra}(\lambda,\rho R_{solar}) = \int_{-\infty}^{+\infty}\int_{0}^{2\pi}\int_{\cos\omega^*}^{1}\int_{0}^{\infty} d\lambda'\, d\varphi\, d\cos\omega\; d(xR_{solar})\times$$

$$N_e(rR_{solar})\times Q_O^{Ra}(\alpha,\Theta)\times$$

$$\frac{1}{2\sqrt{\pi}\Delta b} I(\lambda',\omega,x)\exp\left[-\left(\frac{\lambda-\lambda'\left(1+\frac{2b^2\cos\omega w(rR_{solar})_{radial}}{c}\right)}{2\Delta b}\right)^2\right] \qquad (5.1)$$

where $O \equiv (//,\perp)$

// parallel to the radial plane

$\perp$ perpendicular to the radial plane

$$Q_{//}^{Ra} = \frac{3}{16\pi}\sigma_T\left(\sin^2\alpha + \cos^2\alpha\cos^2\Theta\right)$$

$$Q_{\perp}^{Ra} = \frac{3}{16\pi}\sigma_T\left(\cos^2\alpha + \sin^2\alpha\cos^2\Theta\right)$$

$$b = \cos\gamma = \cos\left(\frac{\pi-\Theta}{2}\right)$$

$$\Delta = \frac{q\lambda'}{c}$$

$$q = \sqrt{\frac{2kT}{m}}$$

$$I\left(\lambda', \omega, x\right) = \frac{1}{\pi}\left(\frac{AU}{R_{solar}}\right)^2\left(\frac{1-u_1+u_1\cos\theta}{1-\frac{1}{3}u_1}\right)f$$

$$\Theta = \pi - \cos^{-1}\left(\sin\omega\sin\varphi\sin\chi + \cos\omega\cos\chi\right)$$

$$\alpha = \sin^{-1}\left(\frac{\sin\omega\sin\varphi}{\sin\left(\pi-\Theta\right)}\right)$$

$$\chi = \cos^{-1}\left(\frac{x}{r}\right)$$

$$\omega^* = \sin^{-1}\left(\frac{1}{r}\right)$$

$$\theta = \sin^{-1}\left(r\sin\omega\right)$$

$$r^2 = x^2 + \rho^2$$

(5.2)

The distances **r**, **ρ** and **x** are expressed in solar radii as follows.

$$\begin{aligned} r &\rightarrow rR_{solar} \\ \rho &\rightarrow \rho R_{solar} \\ x &\rightarrow xR_{solar} \end{aligned} \qquad \textbf{(5.3)}$$

The physical parameters that are inherent in equation (**5.1**) are given in equation (**5.4**).

$$\begin{aligned} &u_1(\lambda') = \text{limb darkening coefficient} \\ &f(\lambda') = \text{extraterrestrial solar irradiance} \\ &N_e(rR_{solar}) = \text{electron density model} \\ &T(rR_{solar}) = \text{coronal temperature model} \\ &W(rR_{solar}) = \text{solar wind model} \end{aligned} \qquad \textbf{(5.4)}$$

The detailed derivation of equation (**5.1**) (=Appendix-**A.98**) is shown in Appendix-**A**. The computer code written in IDL to solve equation (**5.1**) is given in Appendix-**B**. From the physical parameters that are inherent in equation (**5.1**), as shown in equation (**5.4**), it is evident that the shape of the theoretical K-coronal intensity spectrum is dependent upon the models used for the coronal temperature, the solar wind velocity and the electron density distribution structures. In addition the numerical outcome of equation (**5.1**) can also be affected by the numerical methods employed in solving the various integrals. However the extraterrestrial solar irradiance spectrum and the limb darkening coefficients could be considered as well-established quantities. As such, it is prudent to analyze the dependence of the shape of the theoretical K-coronal intensity spectrum on the coronal temperature, the solar wind velocity and the electron density distribution structures and the numerical methods used in solving the integrals.

5.2 Dependence on the electron density distribution function

The bright corona seen during a solar eclipse is due to the scattering of the photospheric light by the free coronal electrons (F-corona), by dust (F-corona) and the emission lines (E-corona). The F-corona can be easily eliminated with the use of polarizes while the E-corona could be identified with the prominent peaks in an otherwise continuous spectrum. These peaks could be easily removed, as demonstrated in figure (**4.33**), to isolate the K-corona. The point that needs to be made here is that the most straightforward way of measuring the coronal electron density distribution is by measuring the K-coronal intensity distribution during a solar eclipse that is filtered through polarizes orientated at three different angles to eliminate the K-corona. This information can then be used to determine the electron density distribution that would have yielded the measured intensity distribution due the scattering of the photospheric spectrum by the free coronal electrons. This method is most suitable for electron density distribution during the maximum phase of the sun, which allows for the corona to assume azimuth symmetry.

One of the pioneering efforts in this regard was due to Baumbach (1937). Baumbach, from an analysis of the photometric material of ten eclipses from 1905 to 1929, deduced the expression given in equation (**5.5**) for the distribution of brightness in the solar corona. This calculation was based upon averaging for all the observations and for all values of the position angle with the brightness of the center of the solar disk taken as 10^6.

$$\mathbf{I(r) = \frac{0.0532}{r^{2.5}} + \frac{1.425}{r^{7.0}} + \frac{2.565}{r^{17.0}}} \qquad \mathbf{(5.5)}$$

From equation (**5.5**) it is apparent from the last term that the brightness falls off most rapidly in the innermost region of the corona while at large distances the brightness is proportional to the first term, which decreases fairly slowly. This formula gives only a smoothed, average value for the distribution of the brightness. On a brighter note November and Koutchmy (1996) report of a best ever achieved white-light coronal observations. This unique opportunity was afforded by the path of total solar eclipse of 11 July 1991 passing above the 3.6 m Canada-France-Hawaii Telescope (CFHT) on Mauna Kea, Hawaii, which allowed for high spatial resolution white-light coronal observations with the most modern detectors that was denied to Baumbach (1937). The sun was at its maximum phase during this eclipse. Like Baumbach (1937), November and Koutchmy (1996) use the sum of three power –law terms to best approximate three regions of the curve, namely, $\mathbf{r}$ < 1.1 SR, 1.1 SR < $\mathbf{r}$ < 1.5 SR, and $\mathbf{r}$ > 1.5 SR (SR = solar radii), to obtain the brightness distribution given by equation (**5.6**). Here again I($\mathbf{r}$) is in units of 10^6 of the solar disk center and ($\mathbf{r}$) in units of solar radii.

$$\mathbf{I(r) = \frac{0.0551}{r^{2.5}} + \frac{1.939}{r^{7.8}} + \frac{3.670}{r^{18.0}}} \qquad \mathbf{(5.6)}$$

Figure (**5.2**) shows the comparison between the brightness distributions given by equation (**5.5**) and equation (**5.6**). November and Koutchmy (1996) conclude that the small difference in the slope to be smaller than the uncertainties in the measurements.

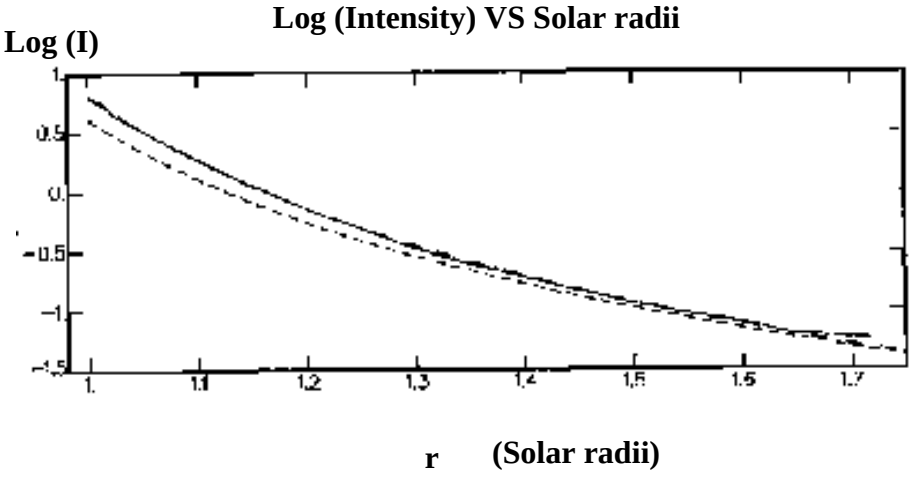

Figure (5.2). A plot showing the solar radial log-intensity variation as a function of solar radii (r) from the center of the sun. The solid curve represents the measurements by November and Koutchmy (1996) while the dashed curve represents the measurements by Baumbach (1937) based on several eclipses observations.

The coronal medium is optically thin. For Thomson scattering in optically thin plasma, the measured K-coronal intensity is proportional to the integral through the line of sight of the electron density times a local dilution factor, which is the solar intensity illuminating the scattering region of the corona. One consequence of this property is that the average radial intensity variation determines the mean radial variation of the electron density. Figure (**5.3**) shows the electron density distribution derived by Baumbach (1937) and November and Koutchmy (1996). Here an isotropic scattering function is assumed. This is not a bad choice for the inner corona since the illumination dilution

factor becomes equivalent to the nearly isotropic scattering form because it represents a superposition of intensity contributions from a wide range of solar disk angles.

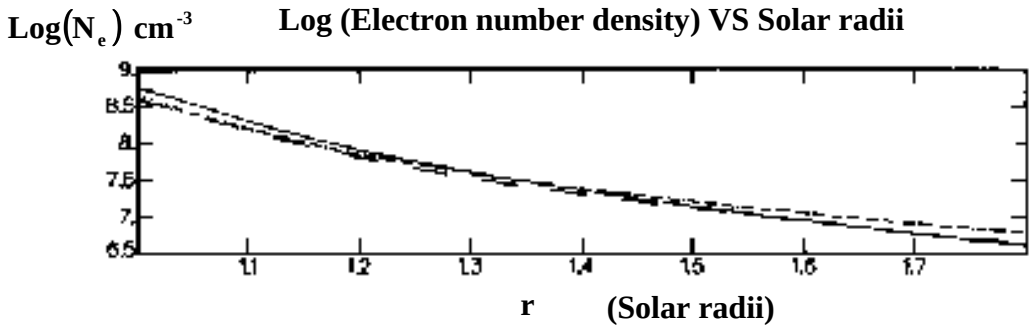

Figure (5.3). A plot showing the log of the electron density variation as a function of the solar radii (r) from the center of the sun. The solid curve represents the calculations by November and Koutchmy (1996) while the dashed curve represents the calculations by Baumbach (1937) based on several eclipses observations.

The electron number density derived by Baumbach (1937) is given by equation (**5.7**). A detailed derivation of equation (**5.7**) is also shown in Shklovskii (1965).

$$N_e(r) = 10^8 \times \left(\frac{0.036}{r^{1.5}} + \frac{1.55}{r^{6.0}} + \frac{2.99}{r^{16.0}}\right) \text{ cm}^{-3} \qquad \textbf{(5.7)}$$

It is true that the total brightness of the corona changes from one eclipse to another. Generally speaking the coefficients of equation (**5.7**) too should change from eclipse to eclipse. At sunspot maximum, that is when the sun is at its maximum phase, the corona has approximately a circular form and uniformly bright as shown in figure (**5.4**). At sunspot minimum, that is when the sun is at its minimum phase, the corona is elongated in the equatorial regions and brighter than the polar regions as shown in figure (**5.5**).

Figure (5.4). A photograph of the solar corona during the total solar eclipse of 11 August 1999 where the sun was approaching the maximum phase. Here the corona is uniformly bright and circular in shape.

Figure (5.5). A photograph of the solar corona during the total solar eclipse of 4 November 1994 where the sun was approaching the minimum phase. Here the corona is elongated in the equatorial regions and brighter than the polar regions.

For several reasons as listed below, the electron number density distribution given in equation (**5.7**) was selected as input parameter in equation (**5.1**) for the computation of the theoretical K-coronal intensity.

(a) This derivation of the electron number density given in equation (**5.7**) was based upon ten eclipse observations. Although the observations were performed almost 60-80 years ago the shape of the density distribution was reconfirmed by November and Koutchmy (1996) using the most modern telescope for the same purpose. Since the reconfirmation was in conjunction with the sun in maximum phase in July 1991, this density distribution could be considered suitable for the total solar eclipse of August 1999, which again coincided with the maximum phase of the sun. The comparison between the electron number densities determined by Baumbach (1937) and November and Koutchmy (1996) is shown in figure (**5.3**).

(b) During the maximum phase of the sun the coronal brightness is approximately uniform all around the sun, which is not true for the sun at the minimum phase where the coronal brightness is concentrated in the equatorial regions. For a sun at the minimum phase a single density distribution function may not hold for all latitudes. Most of the other density models are specific regions and in particular hold for the minimum phase of the sun, which are detailed below. Therefore in conjunction with the maximum phase of the sun where the coronal brightness is uniform all around the sun the density model given by equation (**5.7**) seem to be most appropriate.

(c) The method employed in determining the electron density given by equation (**5.7**) is an average over so many other coronal features. In determining the theoretical K-coronal intensity from equation (**5.1**) it is difficult to integrate over the different coronal features that may cross the line of sight. For such a calculation to be possible individual coronal features have to be identified along with their electron density contrast. In light of the difficulties in such a process it is again most appropriate to use an electron density model averaged over all such coronal features that may occur in conjunction with the maximum phase of the sun.

(d) The very definition of the white-light corona is the brightness produced by the scattering of the photospheric light by the free coronal electrons, which is identified as the K-corona. Although this may be contaminated by the scattering by dust particles, which is identified as F-corona, this contamination can easily quantified by the use of polarizes and eliminated. Also in the region of interest of the experiment described in this dissertation, which is from the limb to 1.5 solar radii, the contribution by F-corona is negligible. Therefore it is prudent to use an electron number density calculation determined by the measurement of the brightness of the white-light corona, which is the case for the electron number density determined by Baumbach (1937) and November and Koutchmy (1996).

The electron density model used Cram (1976), in formulating the properties of the K-coronal intensity spectrum for the determination of the thermal electron temperature in the corona, is given in equation (**5.8**).

$$N_e(r) = 1.67 \times 10^{(4.0+4.04/r)}\ cm^{-3} \qquad \textbf{(5.8)}$$

Ichimoto et al. (1996) used the same electron density model given in equation (**5.8**) in determining the coronal temperatures. Their eclipse observation of February 1994 coincided with the sun at its minimum phase where the coronal brightness is prominently displayed in an elongated shape in the equatorial regions of the sun.

According to Cram (1976) the model given in equation (**5.8**) agrees with the Van de Hulst (1950) minimum equator model within 2% for line of sight between 1.5 and 2.0 solar radii. This model is appropriate for the temperature determination by Ichimoto et al. (1996) because their observations were confined to regions between 1.5 and 2.0 solar radii and also their observations on the total solar eclipse of February 1994 coincided with the minimum phase of the sun.

Another model for the electron number density was due to Newkirk (1961). This model was based on radio and optical observations. Here the effects of refraction were considered while neglecting the effects of magnetic fields. The optical depth effects inherent in any radio observations are discussed in section (**1.2**). Separate values for the electron number densities were obtained for the average corona, the polar caps and the

active regions. The approximate formula for the electron number density presented by Newkirk (1961) is shown in equation (**5.9**).

$$N_e(r) = 4.2 \times 10^{(4.0+4.32/r)}\ cm^{-3} \qquad \textbf{(5.9)}$$

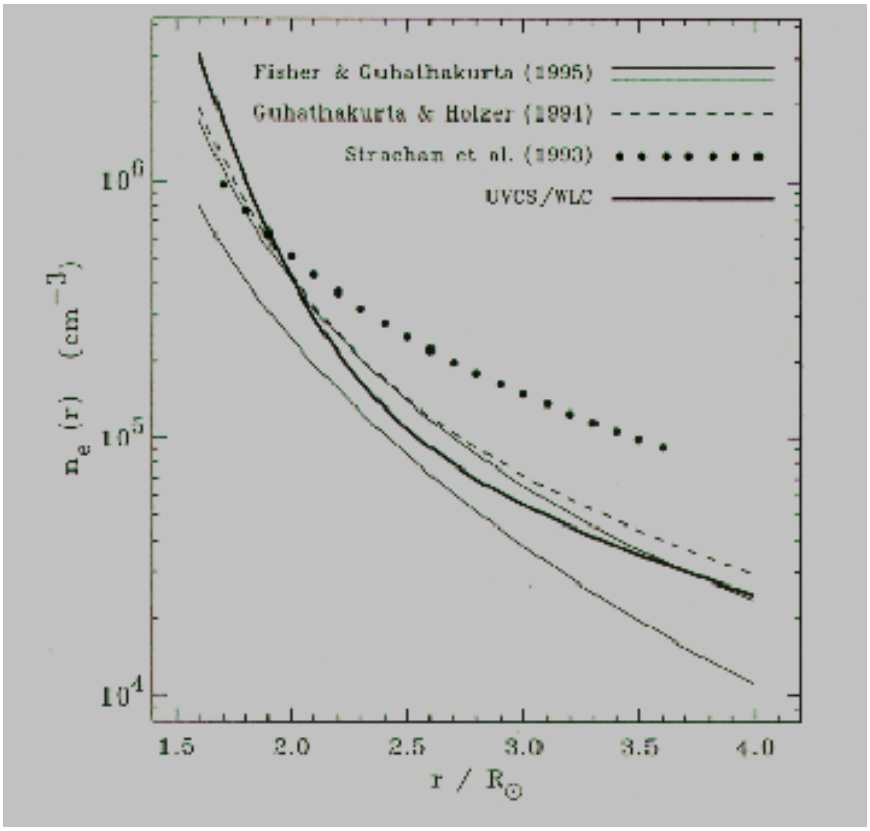

Figure (5.6). A series of plots showing the radial dependence of the mean electron density in coronal holes computed from various sets of polarization brightness data. This plot was obtained from Cranmer et al. (1999).

Various other research groups have computed radial dependence of the mean electron density specific to coronal holes. These calculations were based on various sets K-coronal polarization brightness. Figure (**5.6**) is a plot from Cranmer et al. (1999) showing the electron number density profiles calculated by various research groups.

In figure (**5.6**) the heavy solid line is due to Cranmer et al. (1999) using the UVCS/WLC aboard the SOHO satellite. And the electron number density profile obtained by Cranmer et al. (1999) is given by equation (**5.10**). The observed data in this case is restricted to regions greater than 1.5 solar radii where (**r**) is in solar radii.

$$\mathbf{N_e(r) = 10^8 \times (3.890 \times r^{-10.5} + 0.00869 \times r^{-2.57})\ cm^{-3}} \qquad \mathbf{(5.10)}$$

The filled circles in figure (**5.6**) is due to Strachen et al. (1993) using rocket based coronograph data. Here they considered the corona to be unstructured and spherically symmetric. However this assumption is reasonable for considerations restricted to the coronal hole. Here again electron density profile is restricted to the coronal hole region at heights above 1.5 solar radii. The electron number density profile obtained by Strachen et al. (1993) is given by equation (**5.11**) where (**r**) is in solar radii.

$$\mathbf{N_e(r) = 10^8 \times (0.152 \times r^{-6.71} + 0.0193 \times r^{-2.40})\ cm^{-3}} \qquad \mathbf{(5.11)}$$

Using data obtained by Spartan 201-01, Guhathakurta and Holzer (1994) have presented an electron density profile for the polar coronal hole region specific to the minimum phase of the solar cycle. This again is valid for heights above 2.0 solar radii from the center of the sun. The electron density model by Guhathakurta and Holzer (1994) is given by equation (**5.12**) where (**r**) is in solar radii.

$$\mathbf{N_e(r) = 10^8 \times (0.81 \times r^{-16.87} + 0.80 \times r^{-8.45} + 0.014 \times r^{-2.8})\ cm^{-3}} \qquad \mathbf{(5.12)}$$

The electron density measurements by Fisher and Guhathakurta (1995) were based on the use of both the Mk-III K-coronameter from Mauna Loa and White Light Coronagraph of the space-borne Spartan 201. This study coincided with the maximum phase of the sun in 1990. However the observations were restricted to the northern and southern coronal holes. Their measurements extended from 1.16 solar radii to 5.5 solar radii. The uncertainties reported for the electron density measurements at 1.16 - 1.3 and 1.4 – 1.8 solar radii are ~15% and (30 % - 35 %), respectively. This latter region coincided with data set where Mk-III and Spartan 201 data were cross calibrated. Figure (**5.7**) is a plot of the electron density measurements by Fisher and Guhathakurta (1995).

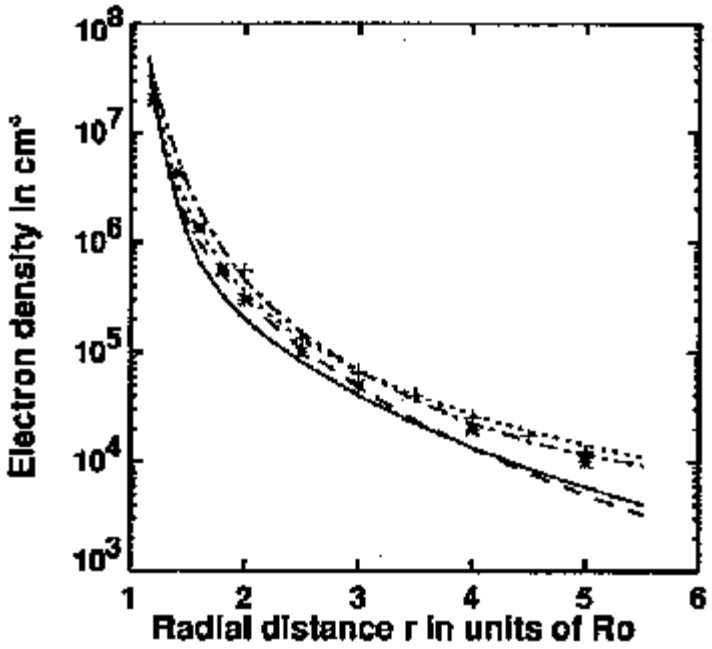

Figure (5.7). A plot showing the electron densities for the north (solid line) and south polar coronal holes (dashed line) and the north (dotted line) and south (dot-dashed line) polar coronal rays as a function of height. Reproduced from Fisher and Guhathakurta (1995).

Figure (**5.8**) is a comparison of the electron number density functions based on the models by Baumbach (1937, equation (**5.7**)), Ichimoto et al. (1996, equation (**5.8**)), Newkirk (1961, equation (**5.9**)), Cranmer et al. (1999, equation (**5.10**)) and Guhathakurta and Holzer (1994, equation (**5.12**)). Figure (**5.9**) is a comparison of the shapes of the K-coronal intensity spectra based on the Baumbach (1937, equation (**5.7**)), Ichimoto et al. (1996, equation (**5.8**)), Newkirk (1961, equation (**5.9**)), Cranmer et al. (1999, equation (**5.10**)) and Guhathakurta and Holzer (1994, equation (**5.12**)) models for the electron number density. These plots are normalized to intensity at 4000.0 angstrom and modeled

for line of sight at 2.0 solar radii above the center of the sun. This plot is simply for the comparison of the shapes of the theoretical K-coronal intensity spectra based on different electron density models. The theory by Cram (1976) for the determination of the thermal electron temperature of the solar corona is based upon the shape of the K-coronal intensity spectrum and not its absolute values. It is evident from figure (**5.9**) that no discernible differences could be seen in the shapes of the theoretical K-coronal spectra for five different electron density models.

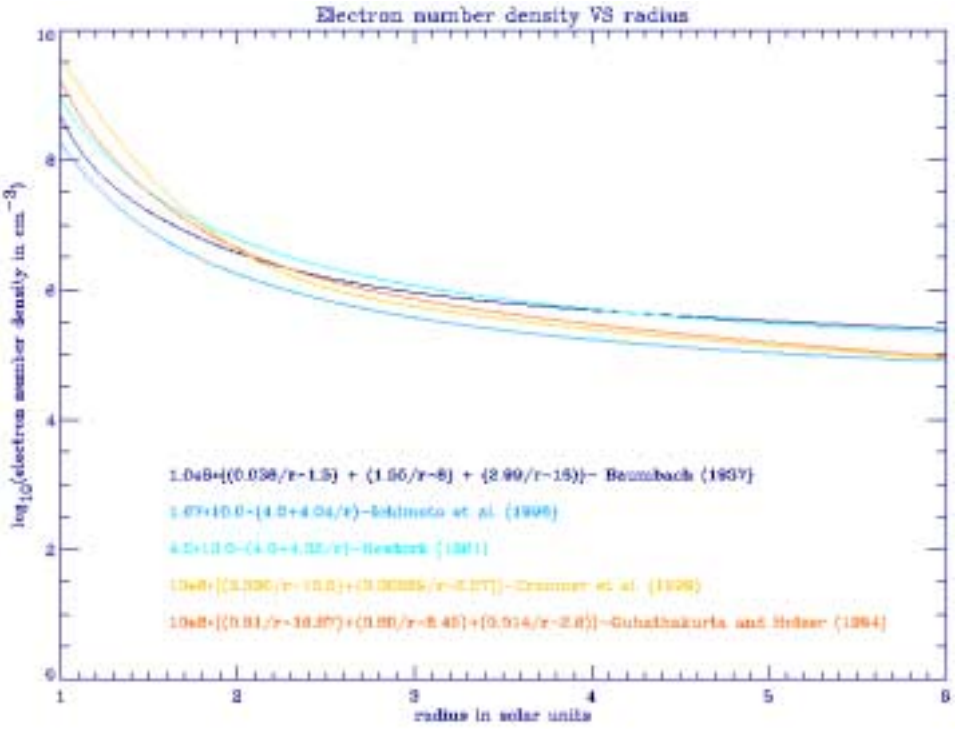

Figure (5.8). A comparison of the electron number density functions based on the models by Baumbach (1937, equation (5.7)), Ichimoto et al. (1996, equation (5.8)), Newkirk (1961, equation (5.9)), Cranmer et al. (1999, equation (5.10)) and Guhathakurta and Holzer (1994, equation (5.12)).

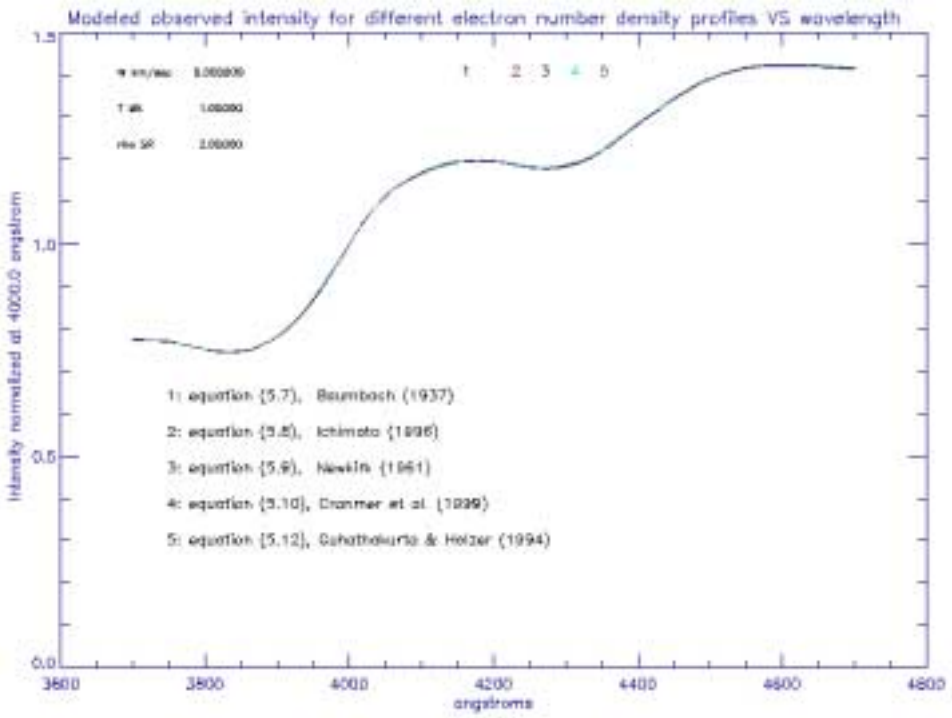

Figure (5.9). Plots of the theoretical K-coronal intensity spectra based on the electron number density functions given by Baumbach (1937, equation (5.7)), Ichimoto et al. (1996, equation (5.8)), Newkirk (1961, equation (5.9)), Cranmer et al. (1999, equation (5.10)) and Guhathakurta and Holzer (1994, equation (5.12)) and the line of sight at 2.0 solar radii from the center of the sun. The curves have been normalized at 4000.0 angstrom.

Figure (**5.10**) is another plot the theoretical K-coronal intensity based on different density models for the line of sight at 1.1 solar radii. Here again no discerning differences could be observed in the shapes of the K-coronal intensity distribution based on the different electron density models. However the absolute values would differ for the different electron density models although it is irrelevant to this experiment.

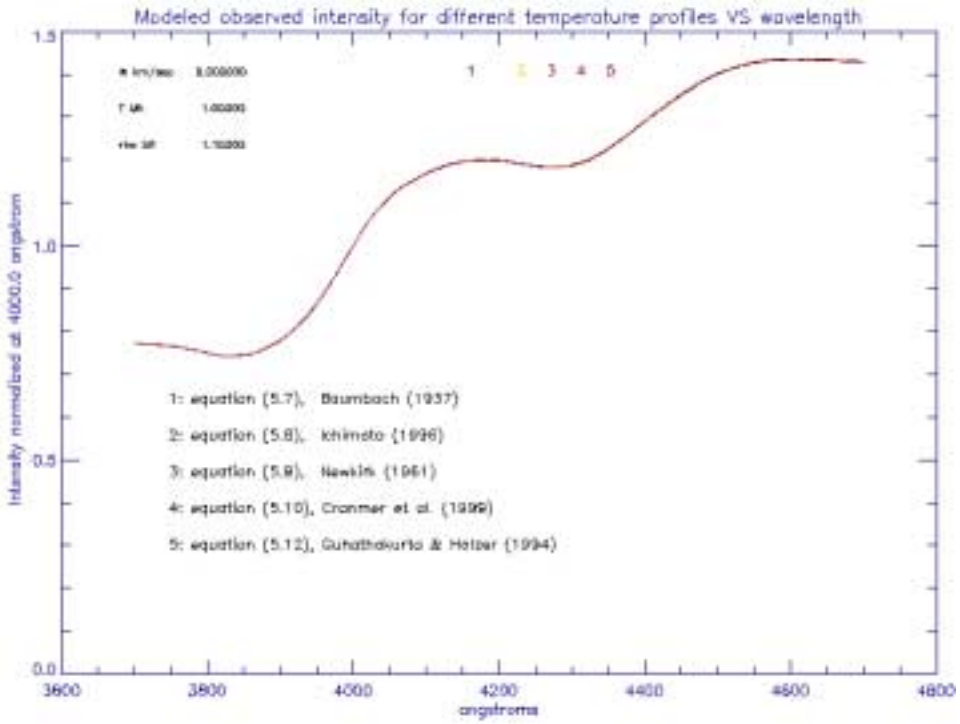

Figure (5.10). Plots of the theoretical K-coronal intensity spectra based on the electron number density functions given by Baumbach (1937, equation (5.7)), Ichimoto et al. (1996, equation (5.8)), Newkirk (1961, equation (5.9)), Cranmer et al. (1999, equation (5.10)) and Guhathakurta and Holzer (1994, equation (5.12)) and the line of sight at 1.1 solar radii from the center of the sun. The curves have been normalized at 4000.0 angstrom.

In summary the electron density measurements given by equations (**5.8**) to (**5.12**) are specific to minimum phase of the sun, or specific to the coronal holes or specific to heights above the region of interest of MACS. The region of interest of MACS extends from 1.1 solar radii to 1.5 solar radii and the experiment coincided with the maximum phase of the sun. In this regard it was decided to select the electron number density given by Baumbach (1937), as given by equation (**5.7**), as input parameter for the theoretical calculation of the K-coronal intensity spectrum. Here the calculations were based on ten

eclipse observations, which avoids the scattering inherent with coronagraphs, and the region of interest extended from 1.0 solar radius to ~3.0 solar radii. Although these measurements were conducted about 60 – 80 years ago, this distribution function was reconfirmed by November and Koutchmy (1996). They had a unique opportunity of performing the same experiment using the most modern 3.6-m CFHT telescope in Hawaii in conjunction with the total solar eclipse of July 1991, where the sun was at its maximum phase.

5.3 Dependence on the temperature profile

Here what need to be investigated are the differences in the theoretical K-coronal intensity profiles based on the assumption of an isothermal corona and temperature profiles with a radial dependence. Usually the radial dependence of the coronal temperature profiles is based on other experimental results. Since the purpose of this dissertation is to determine the temperature and the wind profiles at several coronal heights and latitudes, it will not be helpful in substituting radial temperature profiles determined experimentally. However an important theoretical consideration for the temperature profile of the solar corona is due to Chapman (1957). He assumed that above a certain height in the corona losses by emission to be insignificant compared to conductive losses and derived the following radial dependence for the temperature profile as given by equation (**5.13**) where (**r**) is in solar radii.

$$\mathbf{T(r) = T_0 \times r^{-2/7}} \qquad \textbf{(5.13)}$$

For comparison between an isothermal corona and a temperature profile given by equation (**5.13**) assume the line of sight at 1.3 solar radii with the electron number density profile given by equation (**5.7**). Also assume that for the case of the temperature profile given by equation (**5.13**) that the temperature at the intersection between the line of sight at 1.3 solar radii and the plane of the solar limb to be 1.0 MK and then to fall off as $r^{-2/7}$. For such a case the temperature profile is given by equation (**5.14**) and its variation along the line of sight is given by figure (**5.11**). Here (**r**) is the distance to points along the line of sight from the center of the sun. The isothermal corona assumes a temperature of 1.0 MK all along the line of sight.

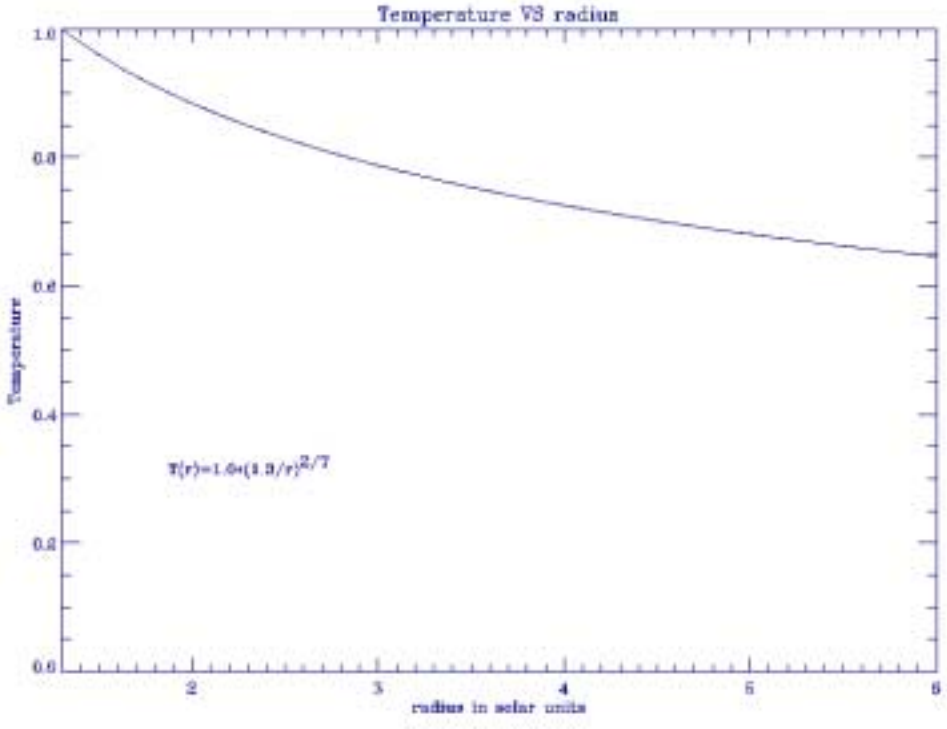

Figure (5.11). This is a plot of the temperature profile along the line of sight at 1.3 solar radii based on the assumption of a conductive corona Chapman (1957). The temperature at the point of intersection of the line of sight and the plane of the solar limb is 1.0 MK.

Figure (**5.12**) is a plot of the theoretical K-coronal intensity spectra due to an isothermal corona of temperature 1.0 MK and due to temperature profiles given by $\mathbf{T(r) = 1.0 \times (1.3/r)^{2/7}}$ and $\mathbf{T(r) = 1.0 + (1.0 + 9.0 * (r - 1.75)^2)^{-1}}$. The latter is a hypothetical temperature profile assumed by Cram (1976). From figure (**5.12**) no discernible differences could be seen between the spectra due to an isothermal corona and the model with a temperature profile given by $\mathbf{T(r) = 1.0 \times (1.3/r)^{2/7}}$.

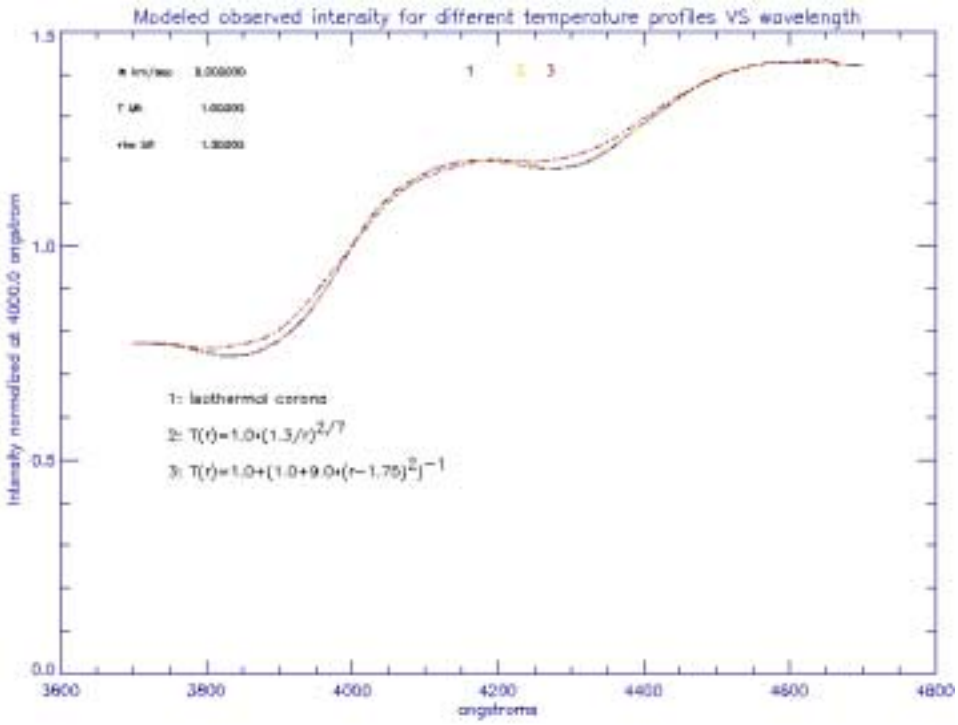

Figure (5.12). This is a plot of the modeled K-coronal intensity spectra for an isothermal corona of 1.0 MK and a model with the temperature profiles given by $\mathbf{T(r) = 1.0 \times (1.3/r)^{2/7}}$ and $\mathbf{T(r) = 1.0 + (1.0 + 9.0 * (r - 1.75)^2)^{-1}}$. Here (r) is the distance between the center and points along the line of sight 1.3 solar radii. The temperature at the point of intersection of the line of sight and the plane of the solar limb is 1.0 MK.

5.4 Dependence on the wind profile

Here again what need to be investigated are the differences in the theoretical K-coronal intensity profiles based on the assumption of an isothermal corona and wind profiles with a radial dependence. Usually the radial dependence of the coronal wind profiles is based on other experimental results. However one important wind profile based purely on theoretical consideration is due to Parker (1958). The wind structures due to isothermal and non-isothermal coronal conditions, driven by sound waves, driven by dust, driven by lines, driven by the combined effect of the magnetic fields and rotation and driven by Alfven waves are detailed in Lamers & Cassinelli (1999).

Consider an isothermal wind in which the gas is subject to two forces: the inward directed gravity and the outward directed gradient of the gas pressure. It has been shown that the momentum equation has many solutions, depending on the boundary conditions but only one of them, the critical solution starts subsonic at the lower boundary of the wind and reaches supersonic velocities at large distances. The solution to the wind structure in such a case is given by equation (**5.14**).

$$\mathbf{v \times \exp\left(\frac{-v^2}{a^2}\right) = a\left(\frac{r_c}{r}\right)^2 \times \exp\left(\frac{-2r_c}{r} + \frac{3}{2}\right) \text{ where } r_c = \frac{GM_{solar}}{2a^2}, \quad a = \sqrt{\left(\frac{RT}{\mu}\right)}} \qquad \textbf{(5.14)}$$

This phenomenon reveals that a wind is generated as a natural consequence of an isothermal corona. In equation (**5.14**), G, T, μ, R, a and $\mathbf{r_c}$ are the universal gravitational constant, isothermal temperature, mean atomic weight of the particles expressed in units of the mass of the proton, universal gas constant, isothermal sound speed and the critical radius, respectively. For solar composition μ is 0.602. For an isothermal temperature of 1.0 MK the isothermal sound speed (**a**) and the critical radius ($\mathbf{r_c}$) are 117.5 km/sec and 6.9 solar radii, respectively. Figure (**5.13**) shows the profile of the wind for the above case.

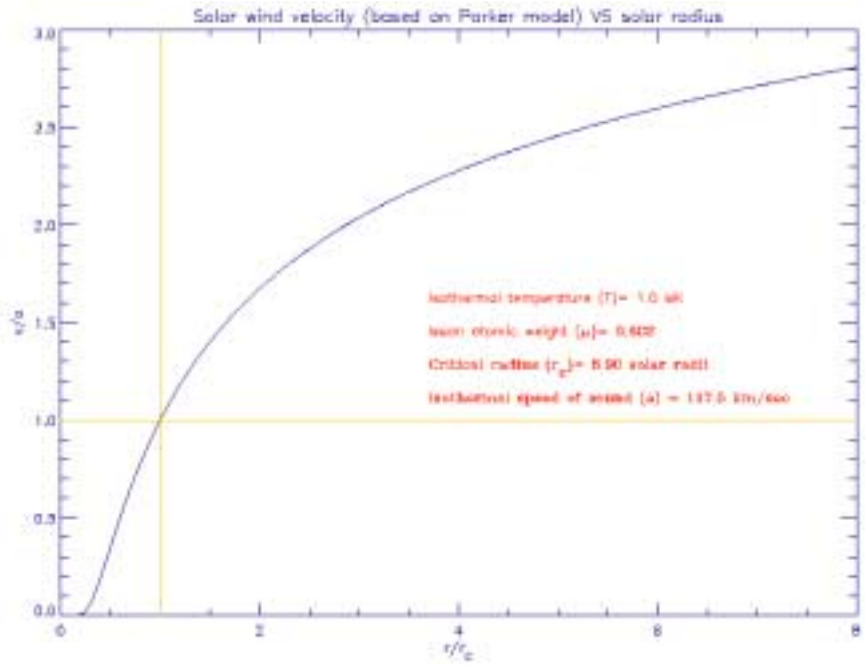

Figure (5.13). Coronal wind profile based on the Parker model for an isothermal corona. In the ideal solution the velocity is equal to the isothermal sound speed at the critical radius and starts with subsonic velocities at the lower boundary and reaches supersonic velocities at large distances.

The Parker wind model shown in figure (**5.13**) is a natural consequence of an isothermal corona. Therefore, even if the solar wind is neglected in the determination for the theoretical K-coronal intensity spectrum for an isothermal corona, it is worthwhile to investigate the effect on this spectrum by the bulk flow velocity introduced by the Parker model naturally. In figure (**5.14**) the comparison is made between a theoretical K-coronal spectrum for an isothermal corona of 1.0 MK, zero wind velocity and line of sight at 1.5 solar radii with the spectrum due to the bulk flow velocity that naturally arises with the introduction of the Parker wind model given in equation (**5.14**).

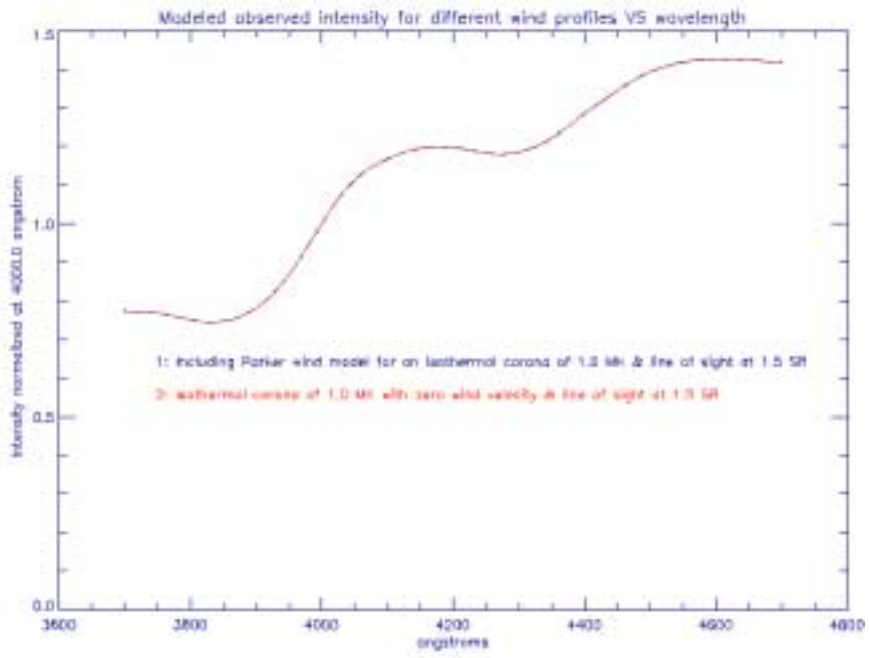

Figure (5.14). Comparison of the theoretical K-coronal intensity spectrum for an isothermal corona at 1.0 MK, zero wind velocity and line of sight at 1.5 solar radii with the intensity spectrum due to the bulk flow velocity that naturally arises with the Parker wind model for an isothermal corona as given in equation (5.14).

In figure (**5.14**) no discernible differences could be observed between the two K-coronal intensity spectra. The reasons for this are twofold. First, from the Parker wind profile shown in figure (**5.13**) it is evident that the solar wind velocity at 1.5 solar radii is very small. Second, although the wind profile shown in figure (**5.13**) indicates that the wind values are significant at large distances, nevertheless, this effect is negligible due to the drop in the electron number density at large distances. Figure (**5.15**) shows the theoretical K-coronal intensity spectra due to isothermal coronal temperatures of 1.0 and 1.5 MK with the inclusion of the Parker wind model for an isothermal corona given in equation (**5.14**). As expected the nodes begin to appear mainly due to the temperature differences.

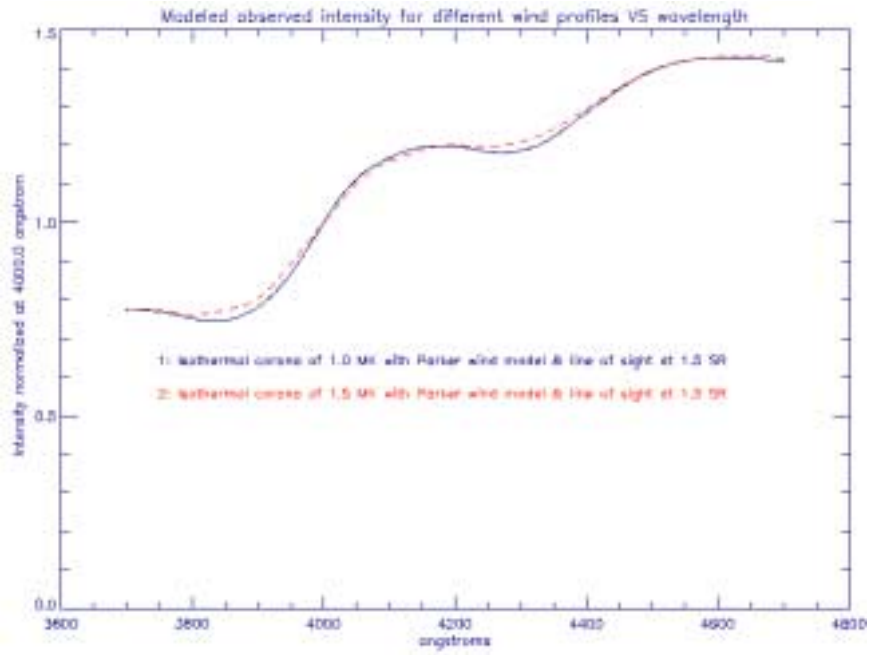

Figure (5.15). Comparison between two theoretical K-coronal intensity spectra due to isothermal coronal temperatures of 1.0 and 1.5 MK and with the inclusion of the Parker wind model for an isothermal corona.

5.5 Dependence on the numerical method

The theoretical model for the K-corona, as shown in equation (**5.1**), consists of four coupled integrations. In the absence of an analytical solution this equation could be solved only through a four-dimensional numerical quadrature. While acknowledging the existence of multitude of numerical methods, the numerical methods used in solving equation (**5.1**) were based on procedures presented in the Handbook of Mathematical Functions (Ed. M. Abromowitz and L.A. Stegun). Two of the integrals were calculated using the Trapezoidal Composite Rule while the other two were solved using a Gaussian Quadrature. There is reason to believe in the results since they can reproduce the theoretical results obtained by Cram (1976) and Ichimoto et al. (1996). This numerical procedure was also sufficient to determine the polarization components to confirm that the degree of polarization is almost wavelength independent and that it increases with heights above the solar limb. The degree of polarization (**p**) is defined by equation (**5.15**).

$$\mathbf{p}(\lambda,\rho) = \frac{\mathbf{I}_{//}^{\mathbf{Ra}}(\lambda,\rho) - \mathbf{I}_{\perp}^{\mathbf{Ra}}(\lambda,\rho)}{\mathbf{I}_{//}^{\mathbf{Ra}}(\lambda,\rho) + \mathbf{I}_{\perp}^{\mathbf{Ra}}(\lambda,\rho)} \quad \textbf{where} \tag{5.15}$$

$$\mathbf{I}_{//}^{\mathbf{Ra}}(\lambda,\rho) = \textbf{Intensity parallel to the radial plane}$$

$$\mathbf{I}_{\perp}^{\mathbf{Ra}}(\lambda,\rho) = \textbf{Intensity perpendicular to the radial plane}$$

Figure (**5.16**) shows a plot of the degree of polarization, for a given isothermal coronal temperature of 1.0 MK, for lines of sight at 1.1, 1.3 and 1.5 solar radii. It is evident from figure (**5.16**) that the polarization components were calculated with sufficient accuracy to confirm the behavior expected of the polarization. That is, they are wavelength independent and increase with heights above the solar limb.

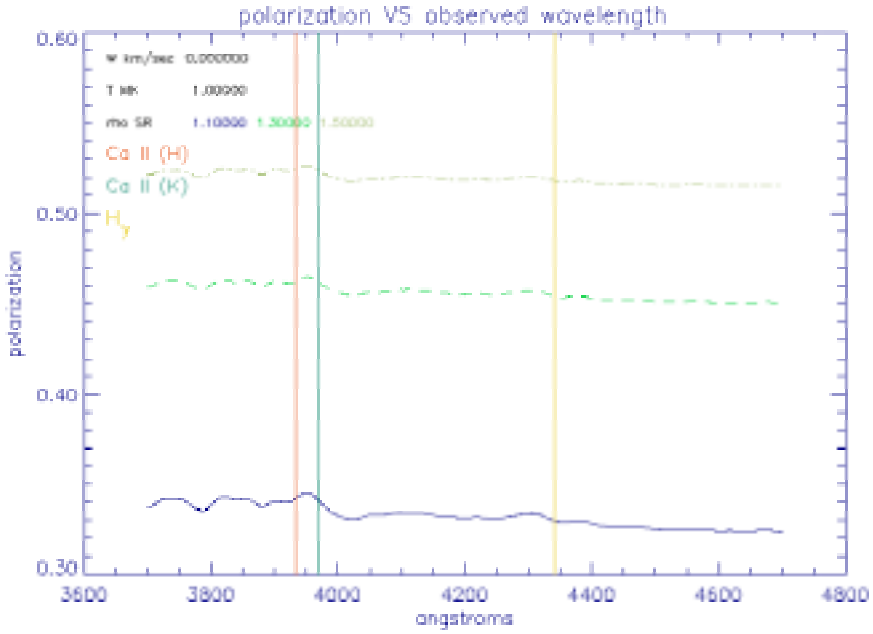

Figure (5.16). Plot of the polarization from theoretical modeling for the formation of the K-corona, at a given isothermal coronal temperature of 1.0 MK, for lines of sight at 1.1, 1.3 and 1.5 solar radii. The behavior of the polarization conforms to the observations. That is, the polarization is almost wavelength independent and increases with coronal heights.

The numerical code to solve equation (**5.1**) was written in IDL (Interactive Data Language) and took ~100 minutes to calculate the intensity spectrum from 3700 – 4700 angstroms in a Pentium-II 233 MHz PC. Of the four integrals two were solved using the Trapezoidal Composite Rule while the other two were solved using Gaussian Quadrature. In the situation where the Trapezoidal Composite Rule was used, the quadrature points were divided into higher and higher number of points to check for differences in the results. The final number of quadrature points was selected based on the point where the overall results for the intensity converges to within five decimal places. As for the other

two integrals, these were solved using Gaussian quadratures. Their integration limits allowed for the use of Hermite polynomials and its associated weights. That is, these integrals had the form given by equation (**5.16**).

$$\int_{-\infty}^{+\infty} f(x)e^{-x^2}dx \approx \sum_{i=0}^{n} f(h_i)w_i \quad \text{where}$$
$$h_i = \text{zeros of Hermite polynomials}$$
$$w_i = \text{weights} \qquad \textbf{(5.16)}$$

However the line of sight integration was of the form given by equation (**5.17**), which was converted to the form given by equation (**5.16**), which follows the procedure given in the Handbook of Mathematical Functions (Ed. M. Abromowitz and L.A. Stegun, pg. 924).

$$\int_{-\infty}^{+\infty} f(x)dx = \int_{-\infty}^{+\infty} \{f(x)e^{+x^2}\}e^{-x^2}dx \approx \sum_{i=0}^{n} \{f(h_i)e^{h_i^2}\}w_i \quad \text{where}$$
$$h_i = \text{zeros of Hermite polynomials}$$
$$w_i = \text{weights} \qquad \textbf{(5.17)}$$

In equation (**5.17**) the function **f(x)** is of the following form given by equation (**5.18**), which is a convergent function without any singularities in the region of interest.

$$f(x) \equiv \left(\frac{0.036}{\left(\sqrt{x^2+\rho^2}\right)^{1.5}} + \frac{1.55}{\left(\sqrt{x^2+\rho^2}\right)^{6}} + \frac{2.99}{\left(\sqrt{x^2+\rho^2}\right)^{16}} \right) \times \frac{1}{\sqrt{x^2+\rho^2}\sqrt{x^2+\rho^2+\mu^2-1}} \qquad \textbf{(5.18)}$$

For example assume μ =1.0 and ρ =1.1 in equation (**5.18**). Then the equation (**5.18**) reduces to equation (**5.19**).

$$\int_{-\infty}^{+\infty}\left(\frac{0.036}{\left(\sqrt{x^2+\rho^2}\right)^{1.5}}+\frac{1.55}{\left(\sqrt{x^2+\rho^2}\right)^{6}}+\frac{2.99}{\left(\sqrt{x^2+\rho^2}\right)^{16}}\right)\times\frac{1}{x^2+\rho^2}dx \qquad \textbf{(5.19)}$$

Solving equation (**5.19**) by using the trapezoidal composite rule, where the integration limit is restricted to $x = \pm 5000$ and dividing this region into 100000 intervals of width 0.1, the result yields a value of 1.1954237. The restriction in the x-range is perfectly valid because the integrand rapidly falls to zero about x=0. Performing this operation over a range of values for μ is very time consuming. However by using the Gaussian quadrature over a Hermite polynomial roots of just twenty points, as specified in equation (**5.17**), the result yields a value of 1.1900812. This value is accurate to within 1.0 % of the result yielded by the trapezoidal composite rule and is also computed very much faster. This is also acceptable in light of the limits imposed by the instrument. An analytical solution also exists for equation (**5.19**) as shown in equation (**5.20**) (Standard Mathematical Tables and Formulae).

$$\int_0^{\infty}\frac{x^a}{\left(m+x^b\right)^c}dx=\frac{m^{\frac{a+1-bc}{b}}}{b}\left[\frac{\Gamma\left(\frac{a+1}{b}\right)\Gamma\left(c-\frac{a+1}{b}\right)}{\Gamma(c)}\right] \qquad \textbf{(5.20)}$$

$$\text{where } a > -1, b > 0, m > 0, c > \frac{a+1}{b},\ \Gamma \equiv \text{Gamma function}$$

Writing equation (**5.19**), as shown in equation (**5.21**), and using equation (**5.20**) yields a value of 1.1954237, which matches with the value obtained by using the trapezoidal composite rule.

$$\int_{-\infty}^{+\infty}\left(\frac{0.036}{\left(\sqrt{x^2+\rho^2}\right)^{1.5}}+\frac{1.55}{\left(\sqrt{x^2+\rho^2}\right)^{6}}+\frac{2.99}{\left(\sqrt{x^2+\rho^2}\right)^{16}}\right)\times\frac{1}{x^2+\rho^2}\,dx$$
$$=2\times\left(0.036\times\int_0^{\infty}\frac{dx}{\left(\rho^2+x^2\right)^{7/4}}+1.55\times\int_0^{\infty}\frac{dx}{\left(\rho^2+x^2\right)^{4}}+2.99\times\int_0^{\infty}\frac{dx}{\left(\rho^2+x^2\right)^{9}}\right) \quad \textbf{(5.21)}$$

The detailed derivation of the theory and the code written in IDL is provided in Appendix – A and B, respectively. Throughout the code the accuracy of the calculations were checked using the built in CHECK_MATH function, which returns the accumulated math error status, and manually. There were no errors reported.